AIAA-2004-0919

MEAN FLOW OF MULTISTREAM RECTANGULAR JETS UNDER NORMAL AND MIXING ENHANCEMENT CONDITIONS

Dimitri Papamoschou *
Thomas T. Dixon †
Kimberley A. Nishi ‡
University of California, Irvine, California 92697-3975

Flow exiting a convergent-divergent nozzle operated at off-design conditions exhibits an instability that causes mixing enhancement in the flow itself and can destabilize an adjacent flow. The latter property enables mixing enhancement of an arbitrary jet via parallel injection of a secondary gas flow. In this study we investigated the effect of mixing enhancement using secondary parallel injection (MESPI) on the mean flow field of rectangular (2D) jets. The mean velocity field was surveyed using an array of Pitot probes. The primary jet was supersonic and the secondary (coflow) jets were high-subsonic. Comparisons were made between MESPI and normal jets for a variety of nozzle arrangements. The most promising configuration utilized coflow on one side only of the primary jet. The bypass ratio was 0.24 and the estimated thrust loss was around 1%. The potential core length was reduced by 60% and the volume flow rate in the mid-field of the jet increased by about 30%. The cross section of the jet evolved rapidly from rectangular to elliptical with axis-switching. Correlation of the mixing rates of all the jets shows that mixing enhancement is sensitive to the area ratio of the secondary nozzle and the recession of the secondary nozzle relative to the primary nozzle. The bypass ratio appears to play minor role.

Nomenclature

A	=	cross sectional area
B	=	bypass ratio, $\dot{m}_2/\dot{m}_1$
D	=	area-equivalent diameter
D_m	=	mass-flux equivalent diameter
F	=	thrust
H	=	exit height
L	=	length of potential core
Q	=	volume flow rate
R	=	recession of coflow nozzle
$\dot{m}$	=	mass flow rate
M	=	ideally expanded exit Mach number
u	=	mean velocity in jet plume
u_m	=	maximum mean velocity ($=u(x,0,0)$)
u_R	=	lowest resolvable mean velocity
U	=	ideally-expanded exit velocity
x	=	axial coordinate
y	=	transverse coordinate
z	=	spanwise coordinate
δ_A	=	area-based jet thickness

Subscripts

1	=	primary flow
2	=	secondary flow (coflow)

*Professor, Associate Fellow AIAA
†Graduate student, Member AIAA
‡Graduate student, Member AIAA

Introduction

The plume of a shock-containing, convergent-divergent nozzle exhibits strong unsteadiness which causes mixing enhancement in the plume itself and can enhance mixing of an arbitrary flow adjacent to the plume. This phenomenon was discovered in coannular jet experiments at U.C. Irvine [1] and was subsequently confirmed in large-scale tests at NASA Glenn Research Center [2]. The method of Mixing Enhancement via Secondary Parallel Injection (MESPI) is characterized by the simplicity of the mixer nozzles and is relevant to combustion and propulsion applications. More recently, MESPI was studied in high-aspect ratio rectangular jets using

centerline pitot surveys and laser-induced fluorescence [3]. These types of jets have increasing relevance to the exhaust of modern military fighters and unmanned aerial vehicles. The present study increases the parameter space of MESPI in rectangular jets and provides a complete mapping of the mean velocity field.

Figure 1 shows the generic geometry of the MESPI nozzle and of the reference nozzle against which the performance of the MESPI nozzle is judged. The primary (inner) flow is the same in both cases; its conditions are irrelevant to the instability mechanism. The secondary (outer) flows of the MESPI and reference nozzles are subjected to the same pressure ratio and are typically compared at the same mass flow rate. For the MESPI nozzle, the duct of the secondary flow is convergent-divergent with exit-to-throat area ratio H_2/H_{2*}. Mixing enhancement occurs when the secondary flow reaches sonic speed at the throat and experiences an adverse pressure gradient near the nozzle exit. The secondary duct of the reference nozzle is convergent. Previous work has shown that mixing enhancement overlaps with the expected occurrence of supersonic nozzle flow separation [1]. The physical mechanisms of MESPI remain unknown and are presently under investigation. Aeroacoustic resonance – a phenomenon similar to screech – has been largely ruled out as the root cause of MESPI [2]. Figure 2 shows representative schlieren images of MESPI in rectangular jets.

If one wishes to include the single jet (primary flow alone) in the comparisons of mixing performance, it is possible to do so by defining a mass-flux-equivalent diameter

$$D_m \;=\; D_1\sqrt{\frac{\dot{m}_1+\dot{m}_2}{\dot{m}_1}} \qquad (1)$$

where subscripts 1 and 2 refer to the primary flow and secondary flows, respectively, and D is the area-equivalent diameter of the primary flow. Normalization of the axial coordinate by D_m scales all the jets to the same mass flow rate. One should keep in mind that the fluid dynamics of the single jet and of the dual-stream jet are very different, even in the absence of MESPI. There is no way for a simple transformation like this to make the two flows totally equivalent. Moreover, the equal-mass-flow-rate scaling holds only in the near field of the jet. In the very far field, a thrust-based diameter makes more sense since the jet origin is reduced to a point force. However, most mixing enhancement applications are concerned with the near field.

Facility and Flow Conditions

High-aspect-ratio rectangular (2D) jets were generated in the triple-stream apparatus depicted in Fig. 3. Exit dimensions of the primary stream were 50.8 mm × 6.35 mm, giving aspect ratio 8.0 and equivalent (area-based) diameter $D_1 = 20.1$ mm. The primary nozzle was designed by the method of characteristics for Mach 1.5 exit flow. The passage for each secondary stream (top and bottom) was formed between the outer wall of the inner nozzle block and the inner wall of the outer nozzle block. The exit of each secondary stream had a width of 50.8 mm (same as that of the primary stream) and variable height H_2. Control of the exit height of each secondary flow was possible by cantilevering the outer blocks to the settling chamber via flexible flat plates. A screw mechanism afixed to the sidewall enabled fine adjustment of the height. The outer nozzle blocks and the flexible plates were replaceable. The convergent segments of all nozzles, and the diverging segments of the outer nozzles, were described by 5-th order polynomials. The length of the flexible plate controlled the recession R of the outer nozzles relative to the inner nozzle.

In this experiment, we used three pairs of secondary nozzle blocks. For fixed exit height H_2 and recession R, each pair gives a unique value of the area ratio H_2/H_{2*}. Two of the coflow nozzle shapes are shown in Fig. 4. Our goal was to assess the effects of area ratio and recession independently while keeping the mass flow rate fixed. This was complicated, however, by the fact that these three parameters are interdependent. The limited number of nozzle blocks, and the finite number of flexible plates, meant that we had to make some compromises in our strategy. Nevertheless, the large number of flows covered, and the proper normalization of the data, allows us to reach certain conclusions about the effects of area ratio, recession, and mass flow rate on the mixing of the jets. Also, we examined the behavior of jets with one coflow only (i.e., only the upper or lower secondary stream was turned on) versus the behavior of jets with two coflows. We will see that the number of coflows plays a critical role in jet mixing.

Table 1 lists the ideally-expanded flow conditions, which were common to all the cases studied here. The primary flow was always at a nozzle pressure ratio NPR_1=3.67 and the secondary flow (one or two streams) was always at a nozzle pressure ratio NPR_2=1.69. The primary flow was ideally expanded with exit Mach number $M_1 = 1.5$. The ideally-

expanded Mach number of the coflow was M_2=0.9. For convergent secondary nozzle this equals the actual exit Mach number. For convergent-divergent secondary nozzle, a shock forms inside the nozzle so the average Mach number at the exit is slightly less than the ideally-expanded value. The Reynolds number of the primary flow, based on H_1, was 570,000. The Reynolds number of the coflow, based on H_2, ranged from 20,000 to 100,000.

Table 2 lists the geometric parameters of each case, the resulting bypass ratio B, the secondary-to-primary thrust ratio, and two global results: the length of the primary potential core and the volume flow rate, to be discussed later in this paper. The notation for each case is B*bbb*A*aaa*R*r* or BB*bbb*A*aaa*R*r*. B indicates a one-stream coflow, BB indicates a two-stream coflow, $bbb = 100 \times B$, $aaa = 100 \times H_2/H_{2*}$, and $r = R/H_1$. For example, B022A141R1 describes a jet with one-stream coflow having bypass ratio $B = 0.22$, area ratio $H_2/H_{2*} = 1.41$ and nozzle recession $R/H_1 = 1$. Convergent coflow nozzles are identified as A100.

Diagnostics

A Pitot rake was used to survey the Pitot pressure in the jet plume. The rake consisted of an aerodynamically shaped aluminum body encasing five stainless steel pitot probes, each 70 mm long. The probes were mounted 10.2 mm apart allowing an overall sampling width of 51 mm. The inlet of each probe had a diameter of 1.0 mm. The rake was mounted on a carriage with motorized motion in the y direction and manual positioning in the x and z directions. For each axial (x) location the rake traversed the plume in the y direction a total of four times. Each time, the rake was moved by a $z-$increment of 2.54 mm, i.e., one fourth of the probe spacing. This resulted in 20 z locations being surveyed for each x. The survey resolution was 2.54 mm in z and 1.0 mm in y. A total of 20-23 $x-$locations were surveyed for each case, with x/H_1 ranging from 0 to 60. Thus, each jet required a total of about 100 traverses of the Pitot rake.

The five probes of the rake were connected individually to five pressure transducers (Setra Model 207). The transducers were mounted on the traverse assembly in order to minimize the length of the tubing between each probe and transducer. This arrangement minimized the response time of the probe-transducer system to values low enough to resolve the sharp spatial gradients in pitot pressure near the nozzle exit. The typical carriage speed was 10 mm/s and the transducers were sampled each at 1000 samples per second by an analog-to-digital board. Each $y-$ traverse resulted in 8000 samples. Mach number and velocity were computed from the pitot pressure assuming constant total temperature (equal to room temperature) and uniform static pressure. In addition to the Pitot pressures, the total pressures of the primary and secondary streams were measured by pressure transducers sampled at the same rate as the Pitot transducers. All seven transducers were calibrated before each experiment.

Noise from the jet was recorded with a 1/2-inch condenser microphone (Brüel & Kjær 4133) located on the sideline of the jet along the minor axis of the nozzle. The frequency response of the measurement was 40 kHz. The microphone data were processed into sound pressure level (SPL) spectra, corrected for microphone response and atmospheric absorption.

Results

Raw Velocity Field

We begin our presentation of the data by plotting isocontours of the velocity field for selected cases. First we show the velocity field on the plane $z = 0$. Figure 5 plots isocontours of $u(x, y, 0)/U_1$ for reference and MESPI cases having two-stream coflows. The MESPI jets have similar area ratios but different recessions. It is evident from the plots that MESPI shortens the potential core (identified by the contour $u(x, y, 0)/U_1 = 0.9$) and shifts all the contours upstream, indicating increased mixing. Also, the edge of the jet is seen to grow faster. A general observation is that the MESPI cases with recessions $R/H_1 = 1$ and 2 generate better mixing than the configuration with zero recession. Figure 6 shows the same arrangements of Fig. 5 but with only one coflow stream. First we note that the mixing of the reference cases was affected little by turning off one of the coflows. Mixing of the MESPI jets is similar to those with two coflows, except for the case with large recession $R/H_1 = 2$ (Fig. 6f). This jet, B024A144R2, grows dramatically faster than its reference counterpart, and it mixing rate exceeds those of all the other MESPI cases.

Figures 7 and 8 show the velocity development on the plane $y = 0$ corresponding to the flows of Figs. 5 and 6, respectively. The reduction in the length

of the potential core of the MESPI jets is again evident. For all the cases, reference and MESPI, we observe a tendency of the momentum flux to concentrate near the jet centerline. This phenomenon is associated with the transformation of the jet cross section from high-aspect-ratio rectangular to circular as we move downstream. The transformation is faster in the MESPI cases and slower in the reference cases. In some cases, for instance B024A144R2 (Fig. 8f), the evolution from rectangular to circular is so fast that the jet slightly contracts in the z direction. This means that the overall mixing rate of case B024A144R2 is not as fast as one would have inferred from xy isocontour of Fig. 6f, although mixing enhancement is still very substantial.

The evolution of the jet cross section becomes clearer in the plots of Figs. 9 and 10, which depict the progression of the isocontours $u(x,y,z)/u(x,0,0)$ for reference and MESPI cases. In Fig. 9 the jets have two-stream coflow and in Fig. 10 they have one-stream coflow. The cross-section of jets with two-stream coflow is symmetric around the $z-$axis and evolves from rectangular to diamond-shape to approximately circular. MESPI accelerates this transition and, at $x/H_1 = 50$, the jet seems to be more elongated in the $y-$direction than in the z-direction. For one-stream coflow, we observe even more dramatic changes between the reference jet and the MESPI jet. The cross section of the refence jet evolves slowly and remains elliptical, with the major axis of the ellipse along the $z-$ direction, all the way to the end of the measurement region. The MESPI jet assumes a triangular cross section near the end of the potential core, with the apex of the triangle on the side of the coflow stream. A short distance downstream, however, the cross section blooms on the side opposite that of the coflow stream. This is also evident in the xy contours of Fig. 6f. Eventually, the cross section becomes elliptic, with the major axis of the ellipse along the $y-$ direction. In other words, this MESPI jet exhibits the phenomenon of axis-switching.

Centerline Velocity

The decay of centerline velocity $u(x,0,0)$ is a relatively simple metric for assessing the mixing rate of a jet. One should be cautious in applying this metric to high-aspect ratio jets because it is possible that the maximum velocity does not occur on the centerline. Examination of the yz isocontours of Fig. 7 and 8, however, indicates that this is not a problem here.

First we plot the axial distributions of $u(x,0,0)/U_1$ versus x/H_1 for all the cases covered here. Figure 11 shows significant variance but, overall, the MESPI cases exhibit faster decay that the normal cases. The SINGLE case lies mid-way between the normal and MESPI jets. To account for the different mass flow rates, we plot in Fig. 12 the same distributions but versus x/D_m. The normal cases collapse fairly well on a single plot. Importantly, the SINGLE case practically overlaps the normal cases. There is still significant variability among the MESPI cases. The normalization x/D_m appears to filter out the effect of mass flow rate, allowing us to make comparisons among cases with different bypass ratios.

It is instructive to examine the differences between normal cases with one and two coflows. Figure 13 plots the centerline velocity of cases BB047A100R0 and B024A100R0. These two cases have identical conditions except that BB047A100R0 has two coflows while B024A100R0 has a single coflow. The SINGLE case is included in the comparison. Remarkably, the distributions of BB047A100R0 and B024A100R0 coincide. The normal jet with single coflow is as stable as the normal jet with two coflows. One would have expected the mixing rate of the normal jet with one coflow to be the average of the mixing rate of the single jet and the mixing rate of the normal jet with two coflows. This argument is based on the expected geometry of the shear layers surrounding the potential core. The fact that the mixing rate of the two jets is practically the same puts in doubt our basic understanding of the connection between the growth rate of an isolated shear layer and the growth rate of the near field of a jet. The same overlap also occurs in cases BB044A100R1 and B022A100R1.

We now examine in more detail the differences between reference and MESPI cases. We concentrate on the "best" cases that produced the fastest mixing with two coflows and with one coflow. Figure 14 compares the best MESPI case with two coflows, its reference case, and the SINGLE jet. In the x/D_m coordinate system the reference jet and the SINGLE jet practically overlap. The potential core of the MESPI jet is 40% shorter than that of the reference jet. Past the ends of their respective potential cores, the decay rates of the MESPI and reference jets are roughly equal. In Fig. 15, we compare the best MESPI case with one coflow, its reference case, and the SINGLE jet. Here the potential core length of the MESPI jet is 60% shorter than that of the

reference jet. The velocity decay past the end of the potential core is faster in the MESPI case. It is evident that MESPI produces superior results when we have only a single coflow.

Thickness and Aspect Ratio

In round jets, it is customary to define the "half-velocity" thickness as the radius at which $u = 0.5u_m$, where u_m is the maximum (centerline) velocity. For rectangular jets obviously there is no such radius. We can, however, define a half-velocity area as the area enclosed by the isocontour $u = 0.5u_m$, as illustrated in Fig. 16. Calling this area $A_{0.5}$, we then define the thickness of an equivalent round jet

$$\delta_A = \sqrt{\frac{4A_{0.5}}{\pi}} \tag{2}$$

The aspect ratio of the jet plume is taken to be the ratio of the width (z) to the height (y) of the isocontour $u = 0.5u_m$. Because of the limited travel of the pitot rake, the $u = 0.5u_m$ isocontour fills the measurement region by about $x/D_m = 8$. Further downstream, parts of this contour lie outside the measurement box, thus preventing computation of the half-velocity area. This is why the thickness and aspect ratio plots terminate at $x/D_m = 8$.

Figure 17 shows the evolution of δ_A for the best MESPI case with two coflows, its reference case, and the SINGLE jet. The faster growth rate of the MESPI case is evident, although in absolute terms the increase in thickness over the reference case is moderate. The thickness of the best MESPI case with single coflow, plotted in Fig. 18, shows a much larger increase over the reference case. Figures 19 and 20 plot the corresponding distributions of aspect ratio. In all cases, the aspect ratio of the MESPI jets reduces more rapidly than the aspect ratio of the reference jets or the single jet. The MESPI case with one coflow displays the fastest reduction, with the aspect ratio reaching 1 at $x/D_m = 8$. Further downstream, the aspect ratio of this jet actually becomes less than one, as indicated by the isocontour plots of Fig. 10.

Volume Flow Rate

A quantitative measure of mixing is the volume flow rate evaluated at a given axial location

$$Q = \int_{A\to\infty} u dA \tag{3}$$

This quantity is always challenging to measure experimentally because it is very hard to resolve the velocity as $A \to \infty$. The difficulty stems from the limit on the dynamic range of the transducer measuring the pitot pressure, which in this case had an accuracy of 0.2% full-scale. This is exacerbated by the extreme sensitivity of velocity on pitot pressure at low values of the pitot pressure. For our experiments, the minimum resolvable velocity was $u_R = 30$ m/s. Some investigations truncate the integration to an area corresponding to the velocity limit. However, this introduces errors in the computation of Q. With increasing distance from the nozzle exit the Pitot pressure drops and, as a result, the dynamic range of the Pitot pressure measurement worsens. For given transducer characteristics, the truncation errors become more severe with increasing axial distance.

A simple method is now described that has the potential to mitigate those errors. Integrating by parts, the volume flow rate is

$$Q = uA\big|_{u=u_m, A=0}^{u\to 0, A\to\infty} - \int_{u_m}^{0} A du \tag{4}$$

For the first term of the right hand side, we consider A as a coordinate that ranges from 0 at the jet centerline, where $u = u_m$, and tends to ∞ at the edge of the jet, where u vanishes. Because u is expected to decay exponentially with A for large values of A, the first term of the right hand side is zero. Thus,

$$Q = \int_0^{u_m} A du \tag{5}$$

In this integral, we treat A as the dependent variable and u as the independent variable. The meaning of $A(u)$ is exemplified by Fig. 16: it is the area enclosed by the isocontour of u. For each value u we have a unique value of A. This relation is plotted in Fig. 21 for one of our measurements. For convenience, the velocity axis is logarithmic. Towards the edge of the jet (specifically, as we approach the lowest resolvable velocity), we observe a linear relation between A and $\ln u$, which confirms the hypothesis that the velocity decays exponentially with A. At the edge of the jet, therefore, we have

$$u = u_0 \exp(-A/A_0) \tag{6}$$

or

$$A = -A_0 \ln(u/u_0) \tag{7}$$

This behavior has been confirmed in all the jet flows and all the axial positions covered in this study. The constants u_0 and A_0 are found by fitting a straight

line, by the method of least squares, through the linear part of the $A - \ln u$ plot. To see how this helps in avoiding truncation errors, we split the integral of Eq. 5 as follows:

$$Q = \int_0^{u_R} A du + \int_{u_R}^{u_m} A du \qquad (8)$$

The first integral is the unresolved part for which A will be approximated by Eq. 7. The second integral is the resolved part. Insertion of Eq. 7 in the first integral yields

$$Q = A_0 u_R \left[1 + \ln(u_R/u_0)\right] + \int_{u_R}^{u_m} A du \qquad (9)$$

This relation was used to compute the volume flow rate. Besides the finite resolution of the pressure transducer, our experiment was also limited in the $y - z$ extent of the measurement region. Beyond about $x/D_m = 8$ a substantial portion of the velocity field lay outside the measurement region. Therefore Eq. 9 could be used reliably only up to $x/D_m = 8$.

Figure 22 shows the evolution of volume flow rate, normalized by the exit value, for the best MESPI case with two coflows, the reference jet, and the SINGLE jet. The plots for the single and reference cases overlap, indicating once again the value of scaling the axial distance with D_m. At $x/D_m = 6$, the MESPI jet offers an increase in volume flow rate of about 24%. For the best MESPI jet with single coflow, Fig. 23, the trends are similar and an increase of 27% in volume flow rate is measured at $x/D_m = 6$. The volume flow rate increases measured here are similar to those obtained in single-stream, Mach 0.3 jets issuing from rectangular lobed nozzles [4].

Overall Trends

Now we attempt to establish correlations of the mixing rate of the jets versus the geometric parameters of the coflow nozzles. Two measures of mixing rate are considered: length of potential core and volume flow rate at $x/D_m = 6$, denoted Q_6. The most relevant geometric parameter is the area ratio H_2/H_{2*} of the coflow nozzle. Given the substantial differences noted between jets with one coflow and two coflows, the correlations are applied separately to each type of jet.

Figure 24 correlates the length of the potential core L_1/H_1 versus the coflow nozzle area ratio. Part (a) includes all the jets with two coflows and part (b) all the jets with one coflow. In both cases, there is a definite trend of reduced potential core length with increasing area ratio. The curves suggest that there may be an asymptotic limit for $H_2/H_{2*} > 1.7$, although the measurements are not sufficient to arrive at definite conclusions. Even though the experiments had large variations in bypass ratio, from 0.06 to 0.48, the near-monotonic trends of Fig. 24 suggest that the bypass ratio does not play a dominant role in mixing enhancement, unless of course it reaches near-zero value.

The normalized volume flow rate Q_6/Q_0 is plotted in Fig. 25. Part (a) includes all the jets with two coflows and part (b) all the jets with one coflow. The general trend indicates an increase in volume flow rate with area ratio, although there is considerable scatter. The peak performance is achieved at area ratio $H_2/H_{2*} \approx 1.4$ with recession $R/H_1 = 1$ for jets with two coflows and $R/H_1 = 2$ for jets with one coflow. These results suggest that nozzle recession produces a definite advantage in rectangular MESPI jets. The optimal recession is not yet known and will be the topic of future studies. It is instructive to examine the relation between volume flow rate and potential core length. Figure 26 plots these two parameters versus each other for all the jets of this study, including the single jet. We observe a definite correlation of increasing volume flow rate with reduced potential core length. Even though there is some scatter, the graph of Fig. 26 indicates that the potential core length (a quantity much easier to measure than the volume flow rate) is a good indicator of the overall mixing rate of the jet.

Noise Spectra

We recorded the noise from several of the flows covered in this study. In some cases, the pitot rake was immersed in the plume and in other cases it was out of the plume. Insertion of the pitot rake did not change the acoustic spectra in any significant way. Figure 27 presents representative results from MESPI and reference cases with two coflows. Both cases exhibit acoustic tones, but the source of the tones is believed to be very different.

The SINGLE jet, which was pressure matched, emitted a moderate screech tone, possibly because of imperfections in the nozzle design that caused weak waves in the jet plume. When two coflows from convergent nozzles were added, the screech tone ampli-

fied. Recall that the coflows are subsonic so they cannot by themselves generate screech. However, the coflow stream direction at the nozzle exit is slightly inward, creating a compression effect on the primary jet. We believe that this gives rise to the screech tone observed in Fig. 27.

For the MESPI jet, we note a sharp tone at a frequency lower than that of the reference jet. It is accompanied by higher harmonics. The tones are believed to be associated with the phenomenon of aeroacoustic resonance inside the convergent-divergent nozzles supplying the coflows [5]. The base level of the spectrum dropped by about 5 dB relative to the reference flow.

As noted in the earlier discussion, the mixing rates of the two cases presented in Fig. 27 are very different, the MESPI jet growing much faster than the reference jet. The fact that both flows had acoustic tones of similar magnitude suggests that the tones are irrelevant to the mixing enhancement process. The same conclusion was reached by the study of Zaman and Papamoschou [2].

Thrust Impact

An issue that invariably arises in this type of investigation is thrust impact of the mixing enhancement method. Here, thrust loss come from the off-design operation of the coflow nozzle. There is currently little information on the details of supersonic nozzle flow separation, especially in moderate expansion nozzles like ours. What we can say with certainty is that one-dimensional theory is inadequate for reliable thrust prediction. Instead, we turn to scarce experimental thrust data available for this flow, summarized in Fig. 28. Plotted is the actual-to-ideal thrust ratio as a function of nozzle area ratio for nozzle pressure ratio 2.0. A least-squares linear fit gives

$$\frac{F}{F_{\text{ideal}}} \approx 1.0 - 0.2\left(\frac{A_e}{A_*} - 1\right)$$

For $A_e/A_* = 1.4$ the thrust ratio is 0.92, hence the thrust loss for the coflow is 8%. This loss should be distributed over the entire jet using the thrust ratio F_2/F_1 in Table 2. The overall thrust loss is 1.8% for BB044A141R1 and 1.1% for B024A144R2. These numbers appear small compared to the losses incurred by mechanical mixers, which tend to be in the 5-to-10 percentile range for the type of supersonic flow examined here [9].

Conclusions

This study solidifies earlier results on the performance of MESPI and provides more details on the mean flow field of multi-stream rectangular jets under normal and MESPI conditions. A large variety of nozzle arrangements was covered. The best configuration utilized coflow on one side only of the primary supersonic jet and provided a reduction of 60% in the length of the potential core and an increase of about 30% in the volume flow rate of the jet. The estimated thrust loss is around 1%.

The results provide guidance for further development of MESPI. It is clear that the dominant variable is the area ratio of the secondary nozzle; however, our data also shows that the recession of the secondary nozzle plays an important role. At the same time, this study underscores the need for improvement in our physical understanding not only of the MESPI phenomenon but also of the "normal" flow. One surprising find is that the normal jet grows at the same rate with one coflow or two coflows. Using conventional arguments one would have expected the jet with two coflows to be more stable than the jet with one coflow. This shows that there are still gaps in our knowledge of the fundamental physics of the near-field growth process.

The physics of MESPI are now being addressed in a special facility designed to study supersonic nozzle flow separation. Early results indicate that the MESPI instability may be caused by asymmetric formation of the shock wave inside the nozzle, although many details of the flow still need to be investigated to arrive at firm conclusions [10].

Acknowledgements

The support by NASA Glenn Research Center is gratefully acknowledged (Grant NAG-3-2345 monitored by Dr. Khairul Zaman). The method of mixing enhancement using axial flow is proprietary to the University of California and is protected by a U.S. patent.

References

[1] Papamoschou, D., "Mixing Enhancement Using Axial Flow," AIAA-2000-0093.

[2] Zaman, K.B.M.Q, and Papamoschou, D., "Study of Mixing Enhancement Observed with a Co-Annular Nozzle Configuration, " AIAA-2000-0094.

[3] Murakami, E. and Papamoschou, D., "Experiments on Mixing Enhancement in Dual-Stream Jets," AIAA-2001-0668.

[4] Zaman, K.B.M.Q, Wang, F.Y., and Georgiadis, N.J., "Noise, Turbulence, and Thrust of Subsonic Freejets from Lobed Nozzles," *AIAA Journal*, Vol. 41, No.3, 2003, pp. 398-407.

[5] Zaman KBMQ, Dahl MD, Bencic TJ, Loh CY, "Investigation of a 'Transonic Resonance' with Convergent-Divergent Nozzles," *Journal of Fluid Mechanics,* Vol. 463, July 2002, pp. 313-343.

[6] Miller, E.H., and Migdal, D., "Separation and Stability Studies of a Convergent-Divergent Nozzle," *AIAA Journal of Aircraft*, Vol. 7, No.2, 1970, pp. 159-163.

[7] Wilmoth, R.G., and Leavitt, L.D., "Navier Stokes Predictions of Multifunction Nozzle Flows," *Society of Automotive Engineers Transactions*, Vol. 96, Sec.6, Paper 871753, 1987, pp. 6.865-6.879.

[8] Hunter, C.A., "Experimental, Theoretical and Computational Investigation of Separated Nozzle Flows," AIAA-98-3107.

[9] Zaman, K.B.M.Q., "Jet Spreading Increase by Passive Control and Associated Performance Penalty," AIAA-99-3505.

[10] Papamoschou, D. and Zill, A., "Supersonic Nozzle Flow Separation, " AIAA-2004-1111.

Table 1 Flow conditions

Quantity	Primary	Secondary
Nozzle pressure ratio	3.67	1.69
Mach number	1.50	0.90
Velocity (m/s)	430	290

Table 2 Geometric parameters and global results

Case	H_2/H_1	H_2/H_{2^*}	R/H_1	B	F_2/F_1	D_m/H_1	L_1/H_1	Q_6/Q_0
SINGLE	0.00	1.00	-	0.00	0.00	3.19	13.8	2.17
BB047A100R0	0.44	1.00	0.0	0.47	0.32	3.88	16.9	2.21
B024A100R0	0.44	1.00	0.0	0.24	0.16	3.55	17.5	2.22
BB022A100R0	0.20	1.00	0.0	0.22	0.15	3.52	14.2	2.08
B011A100R0	0.20	1.00	0.0	0.11	0.07	3.36	16.3	2.15
BB039A124R0	0.44	1.24	0.0	0.39	0.26	3.76	12.8	2.23
B019A124R0	0.44	1.24	0.0	0.19	0.13	3.49	10.9	2.33
BB012A168R0	0.20	1.68	0.0	0.12	0.08	3.39	10.1	2.33
B006A168R0	0.20	1.68	0.0	0.06	0.04	3.29	10.5	2.51
B011A140R0	0.28	1.40	0.0	0.11	0.07	3.36	11.6	2.58
BB044A100R1	0.42	1.00	1.0	0.44	0.30	3.85	15.2	2.12
B022A100R1	0.42	1.00	1.0	0.22	0.15	3.53	16.2	2.06
BB044A141R1	0.57	1.41	1.0	0.44	0.30	3.82	9.3	2.63
B022A141R1	0.57	1.41	1.0	0.22	0.15	3.53	10.5	2.45
BB049A107R2	0.48	1.07	2.0	0.49	0.33	3.90	15.8	2.30
B024A107R2	0.48	1.07	2.0	0.24	0.16	3.55	14.8	2.26
BB049A144R2	0.65	1.45	2.0	0.49	0.33	3.89	11.3	2.36
B024A144R2	0.65	1.45	2.0	0.24	0.16	3.56	8.7	2.81

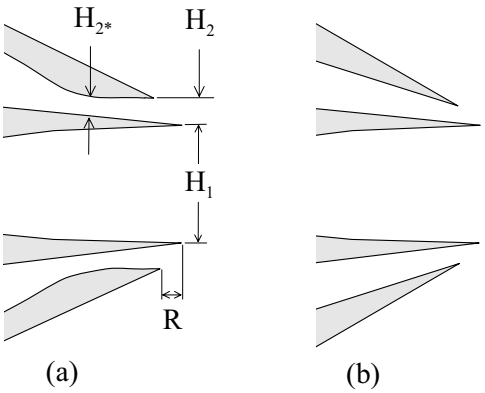

Figure 1: Generic geometry of (a) MESPI nozzle and (b) reference nozzle. The inner streams are identical; the outer streams are supplied at the same pressure ratio and typically at the same mass flow rate.

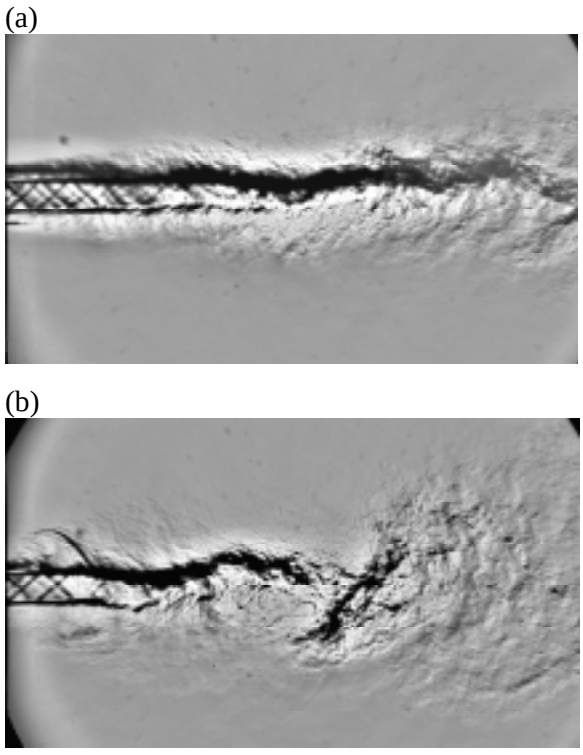

Figure 2: Spark schlieren images of rectangular jets from (a) reference nozzle; (b) MESPI nozzle.

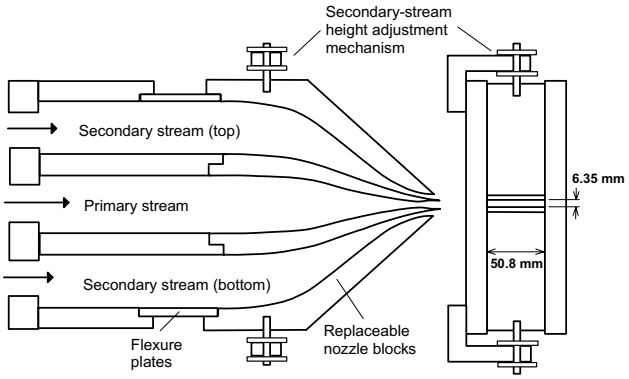

Figure 3: High-aspect-ratio rectangular (2D) triple-stream jet facility.

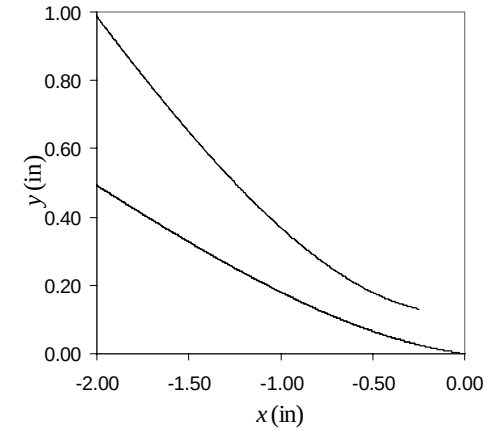

Figure 4: Coordinates of nozzle termination of two of the arrangements used in this study. (a) Reference; (b) MESPI.

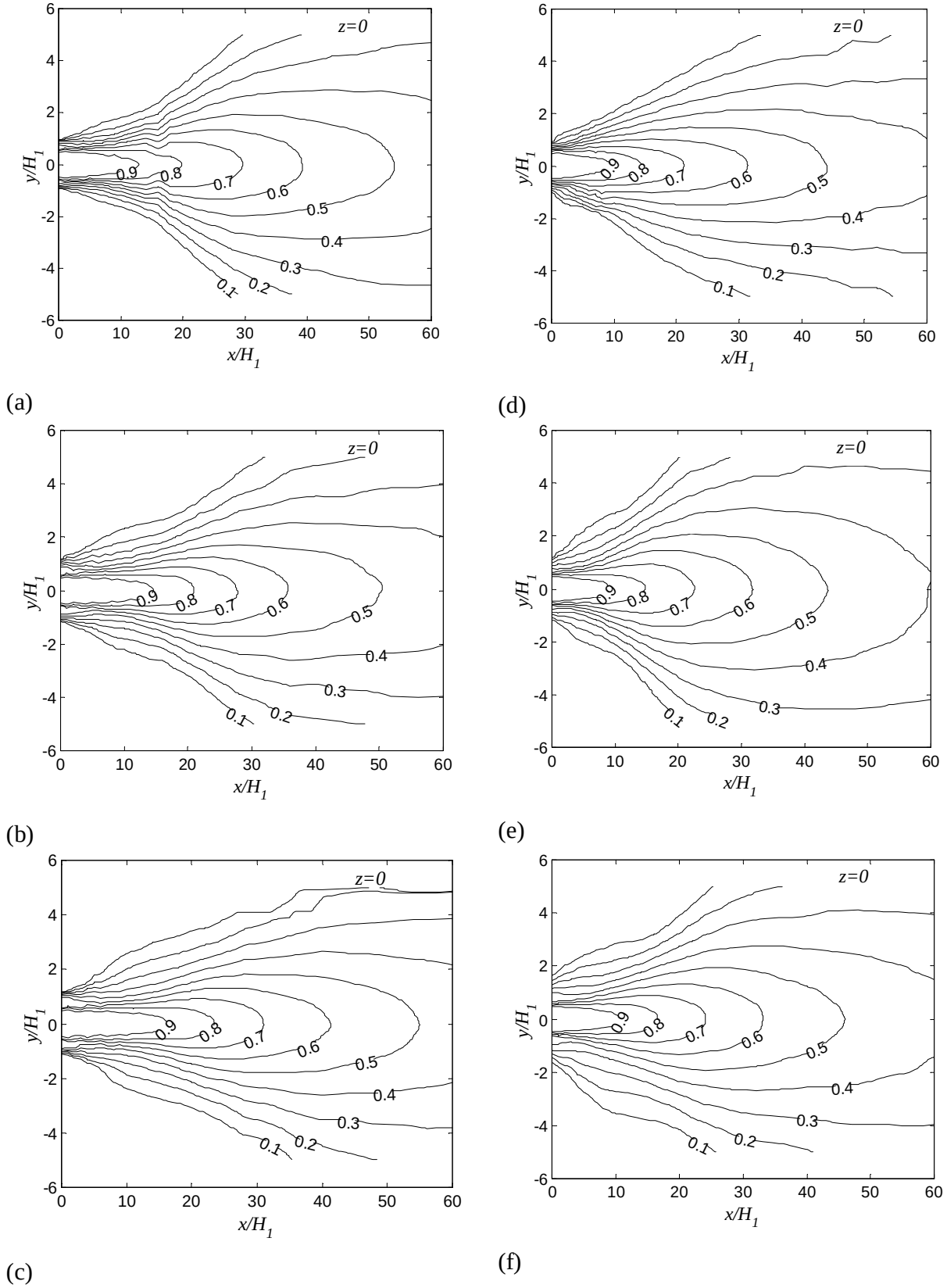

Figure 5: Isocontours of $u(x, y, 0)/U_1$ for cases with two coflows. Left column shows the reference cases and right column shows the corresponding MESPI cases. (a) BB022A100R0; (b) BB044A100R1; (c) BB047A100R0; (d) BB012A168R0; (e) BB044A141R1; (f) BB049A144R2.

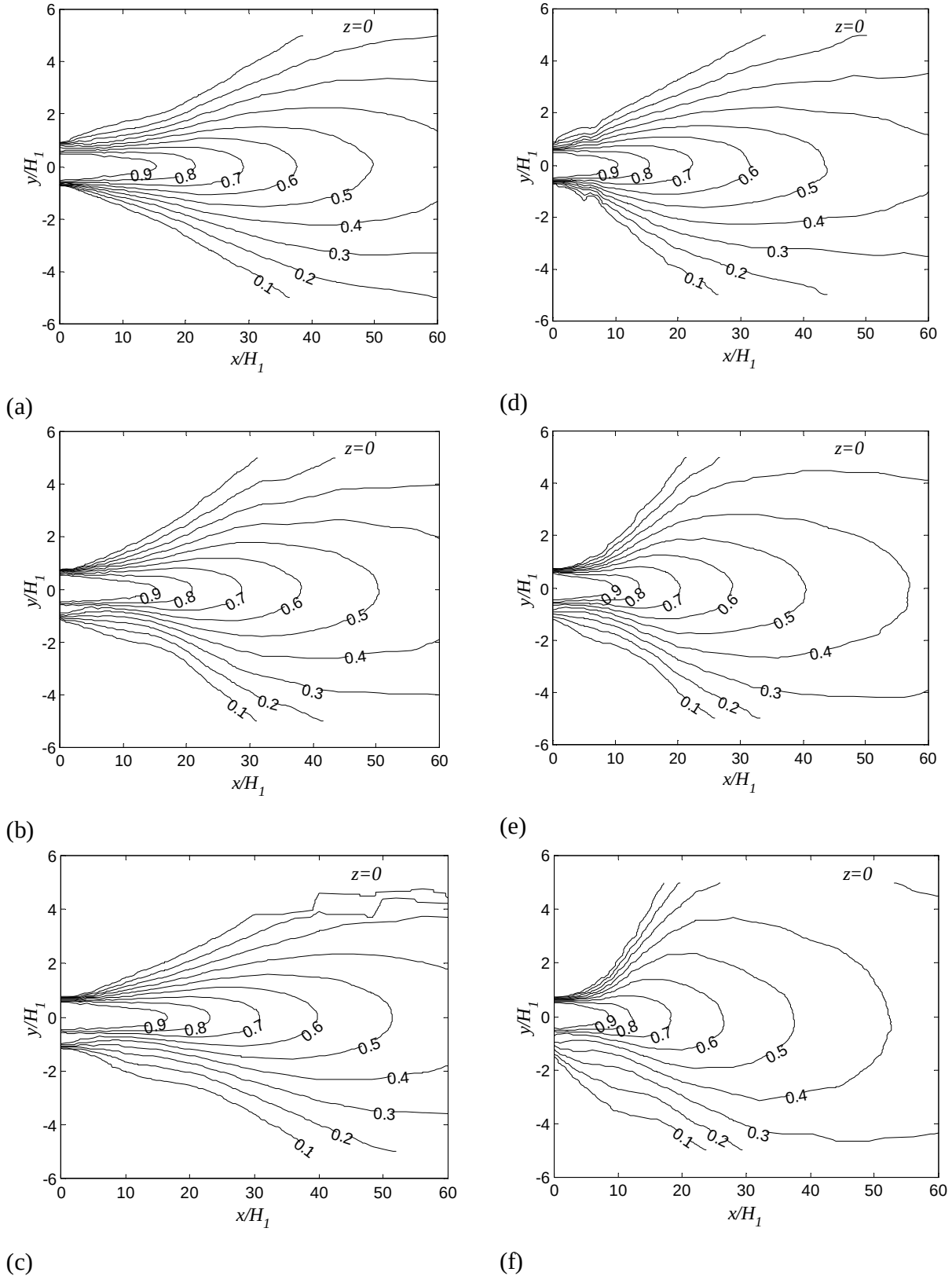

Figure 6: Isocontours of $u(x, y, 0)/U_1$ for cases with one coflow. Left column shows the reference cases and right column shows the corresponding MESPI cases. (a) B011A100R0; (b) B022A100R1; (c) B024A100R0; (d) B006A168R0; (e) B022A141R1; (f) B024A144R2.

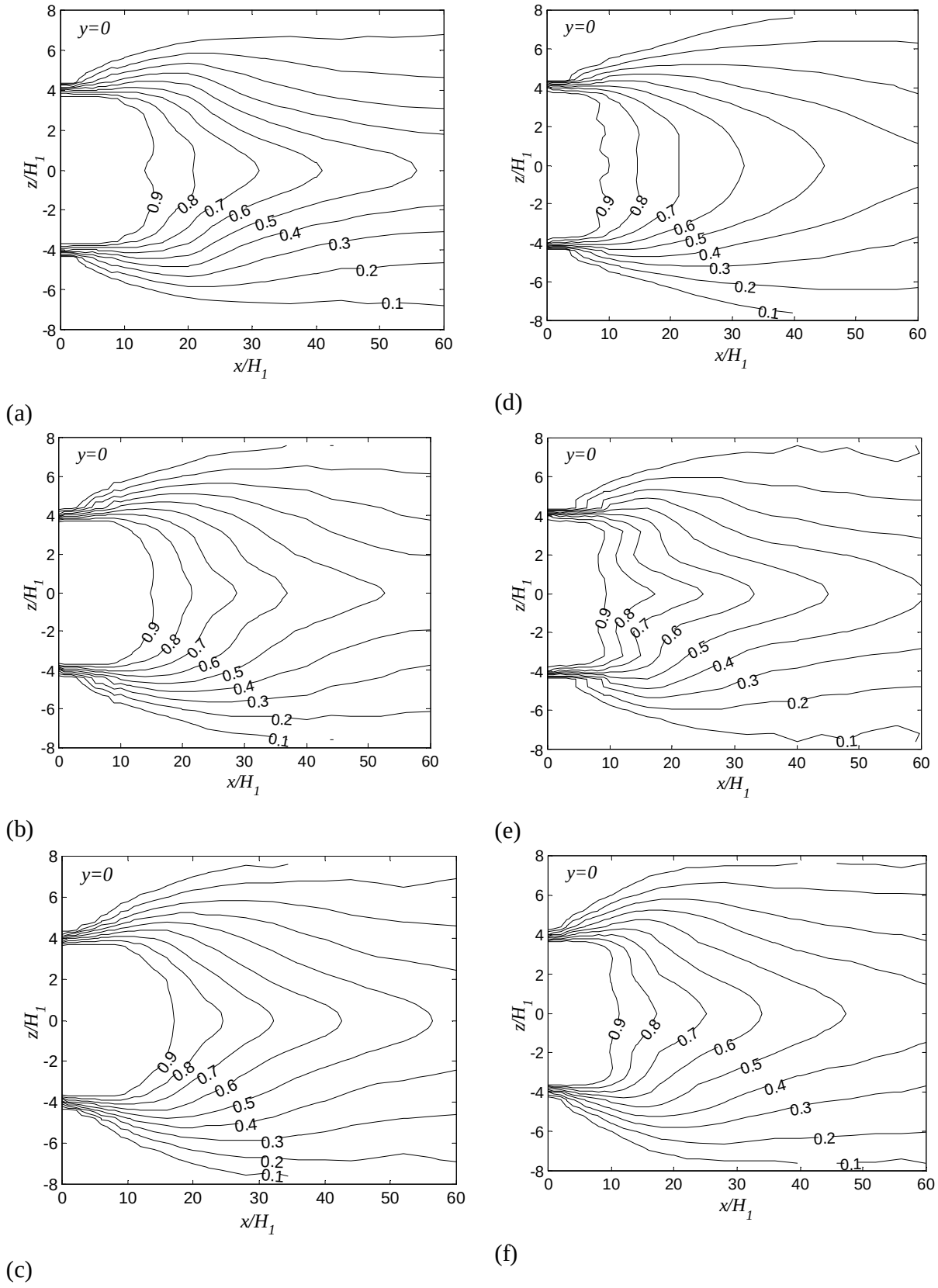

Figure 7: Isocontours of $u(x, 0, z)/U_1$ for cases with two coflows. Left column shows the reference cases and right column shows the corresponding MESPI cases. (a) BB022A100R0; (b) BB044A100R1; (c) BB047A100R0; (d) BB012A168R0; (e) BB044A141R1; (f) BB049A144R2.

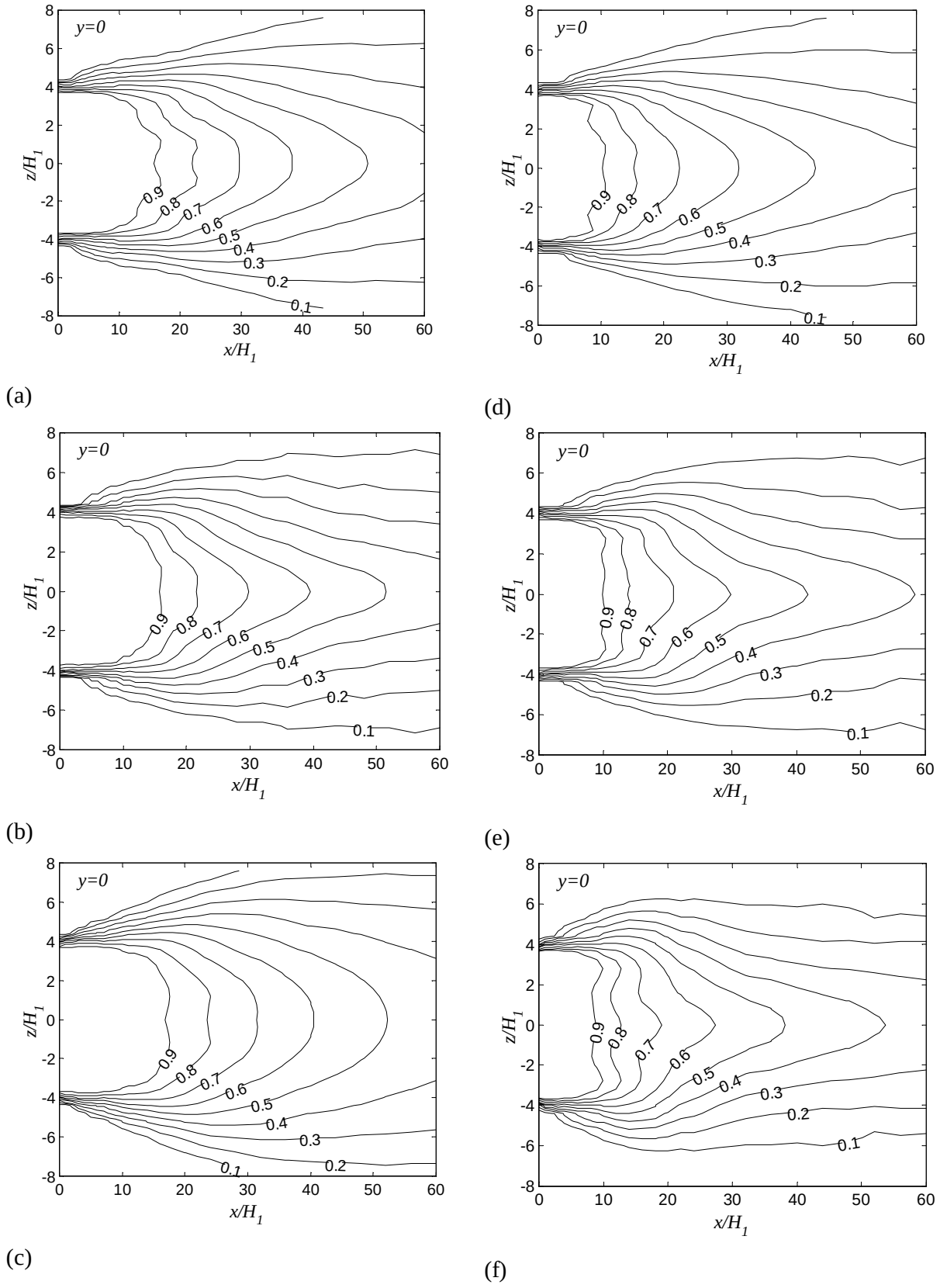

Figure 8: Isocontours of $u(x, 0, z)/U_1$ for cases with one coflow. Left column shows the reference cases and right column shows the corresponding MESPI cases. (a) B011A100R0; (b) B022A100R1; (c) B024A100R0; (d) B006A168R0; (e) B022A141R1; (f) B024A144R2.

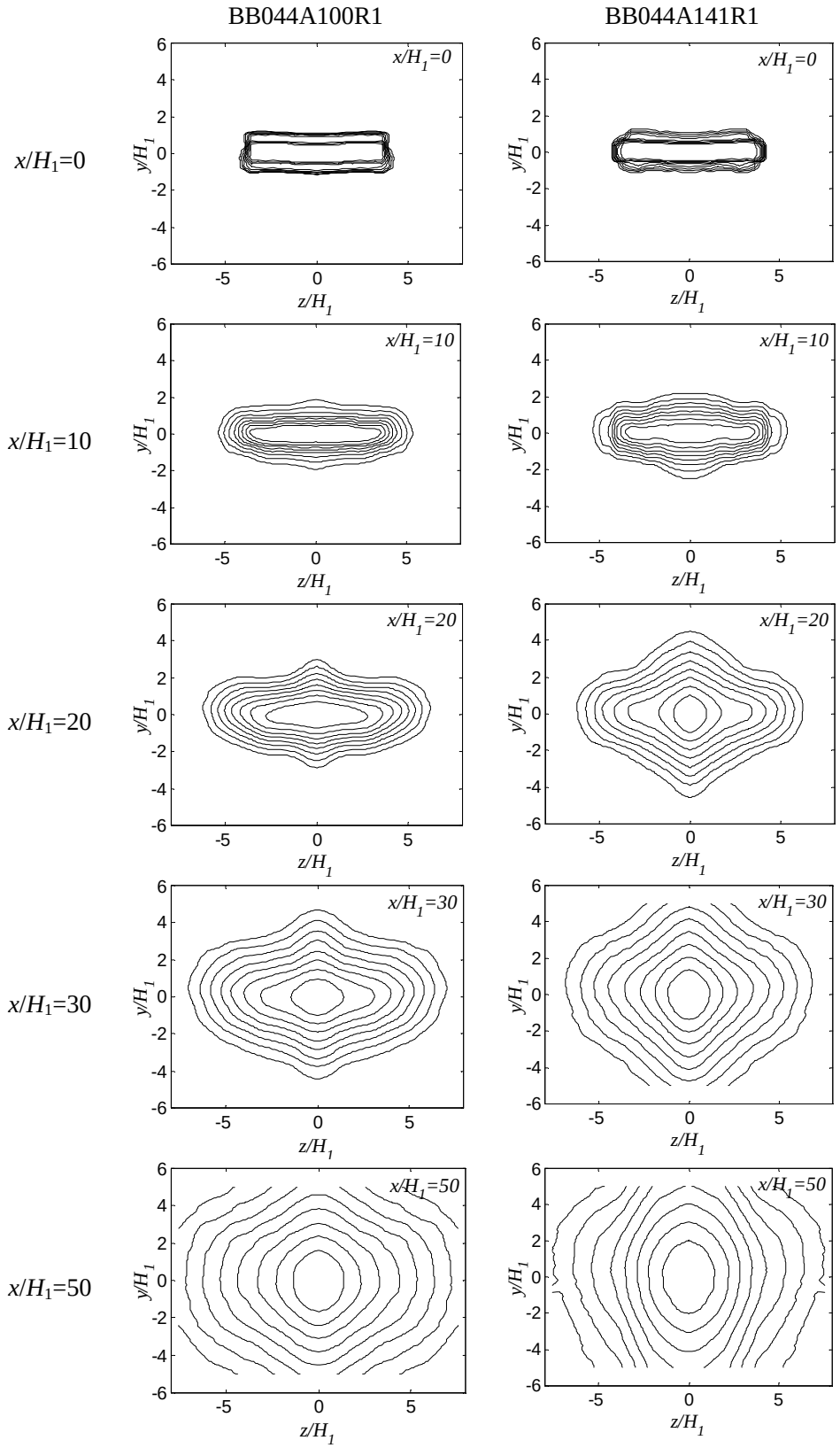

Figure 9: Axial progression of isocontours of $u(x, y, z)/u(x, 0, 0)$ for cases with two coflows. Left column shows the reference case and right column shows the corresponding MESPI case.

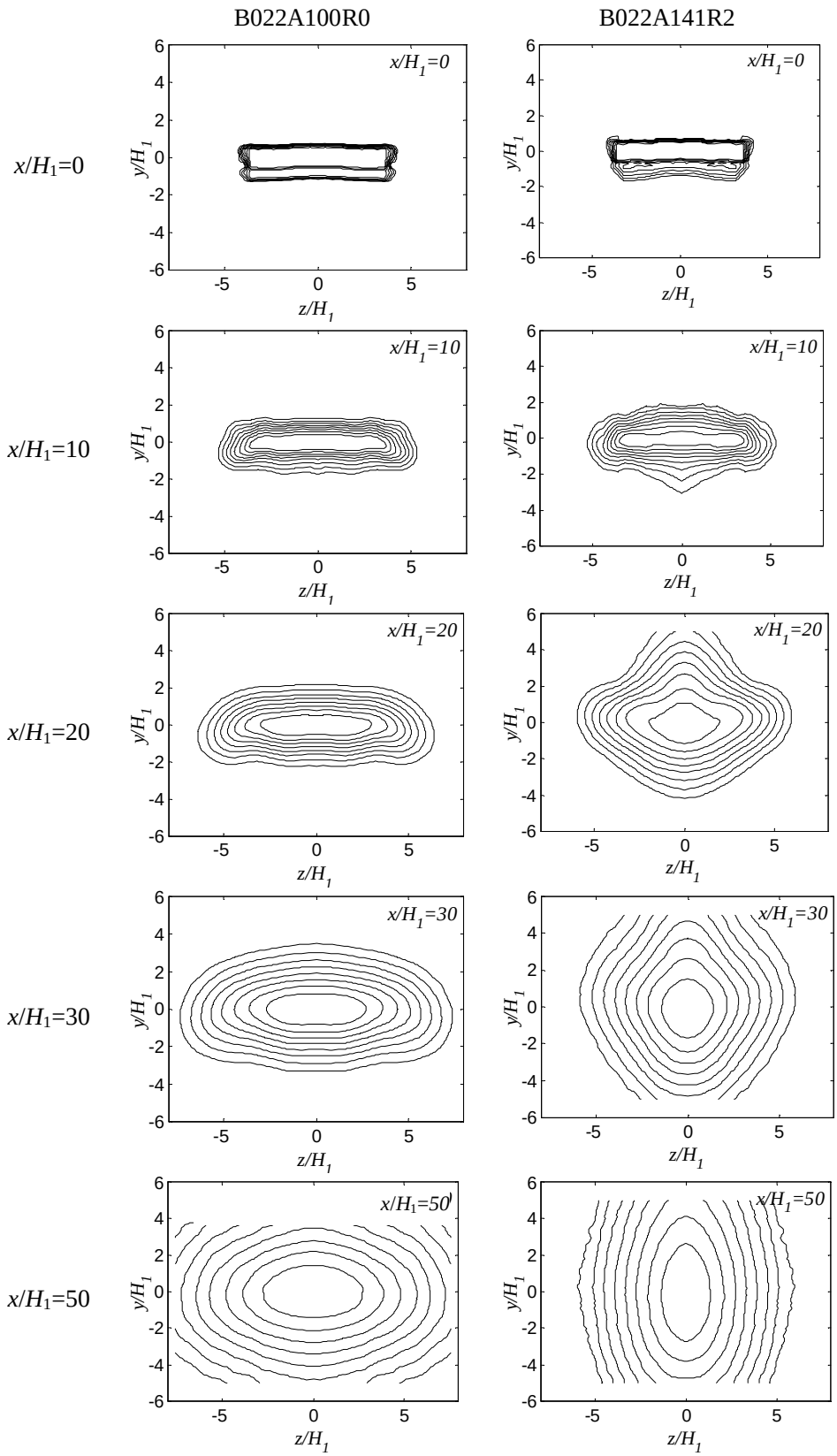

Figure 10: Axial progression of isocontours of $u(x,y,z)/u(x,0,0)$ for cases with one coflow. Left column shows the reference case and right column shows the corresponding MESPI case.

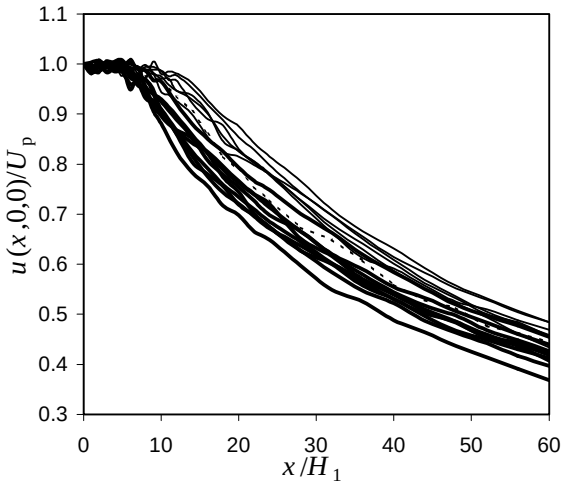

Figure 11: Centerline velocity distributions of all cases. Comparison is done on an absolute basis. Thin lines represent normal flows, heavy lines represent MESPI flows, and dashed line represents the SINGLE jet.

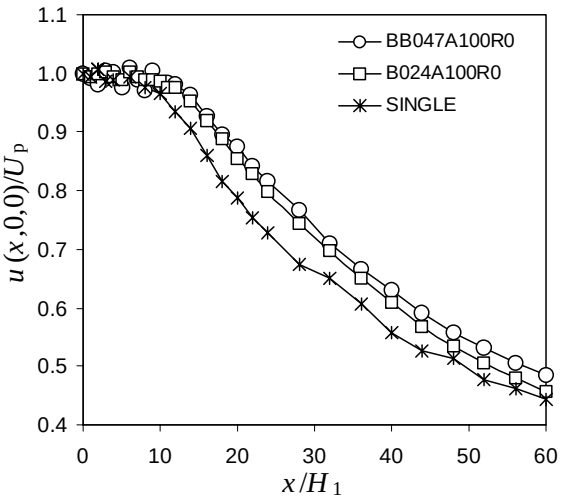

Figure 13: Centerline velocity distributions in absolute frame. Comparison is made between normal cases with one coflow and two coflows, the coflows being identical. The SINGLE case is also plotted.

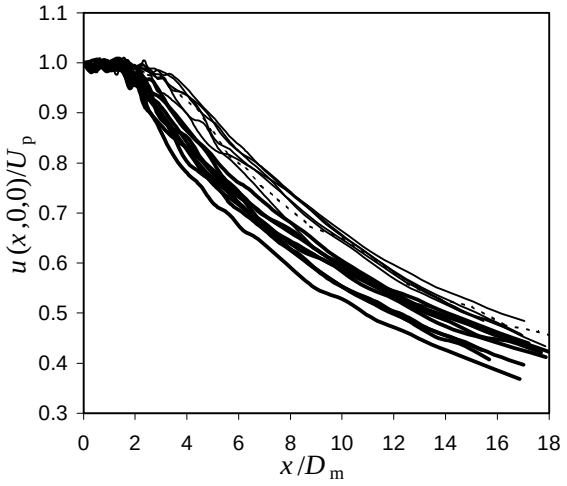

Figure 12: Centerline velocity distributions of all cases. Comparison is done on an equal-mass-flux basis. Thin lines represent normal flows, heavy lines represent MESPI flows, and dashed line represents the SINGLE jet.

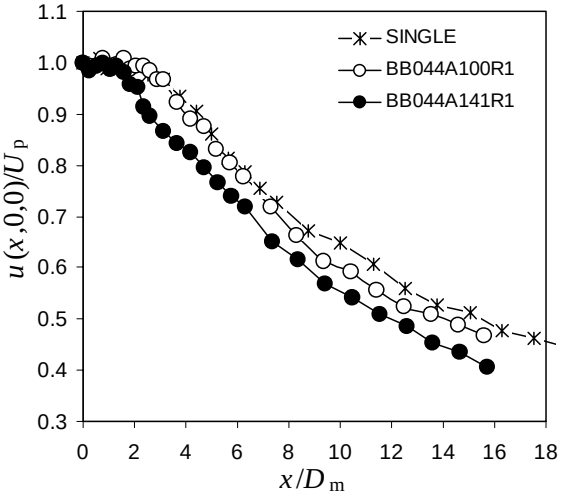

Figure 14: Centerline velocity distributions in x/D_m frame. Comparison between MESPI case with two coflows, reference case, and SINGLE jet.

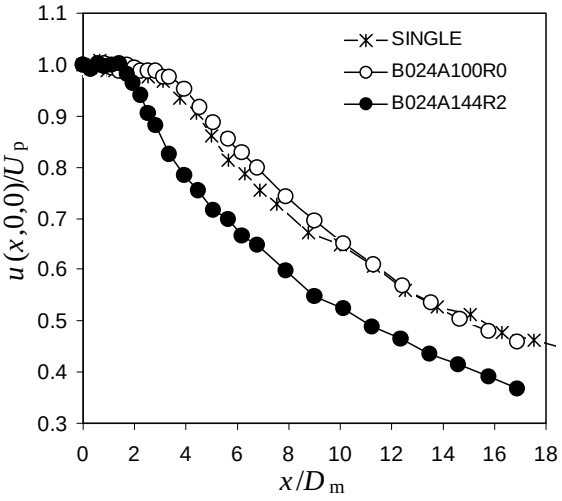

Figure 15: Centerline velocity distributions in x/D_m frame. Comparison between MESPI case with one coflow, reference case, and SINGLE jet.

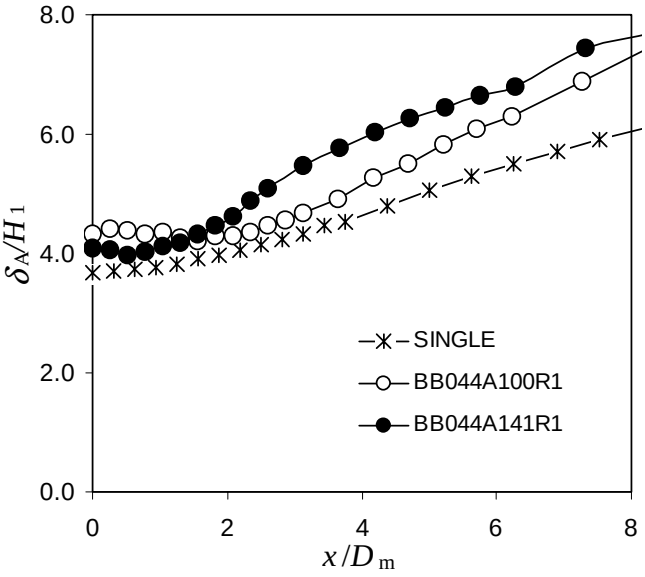

Figure 17: Evolution of area-based thickness. Comparison between MESPI case with two coflows, reference case, and SINGLE jet.

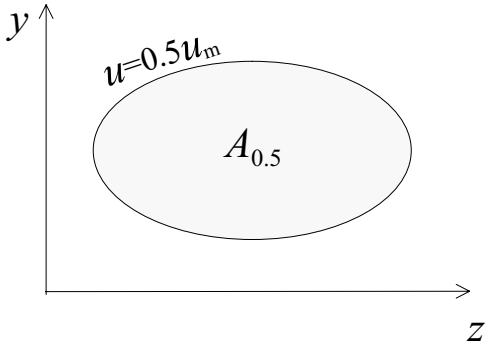

Figure 16: Definition of half-velocity area. Aspect ratio is the width (z) over the height (y) of the $u = 0.5u_m$ isocontour.

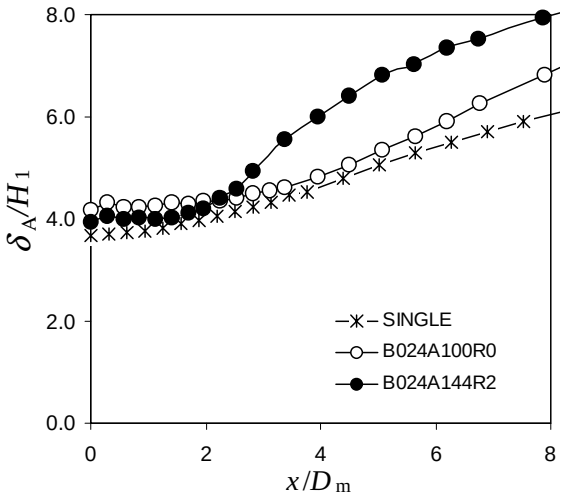

Figure 18: Evolution of area-based thickness. Comparison between MESPI case with one coflow, reference case, and SINGLE jet.

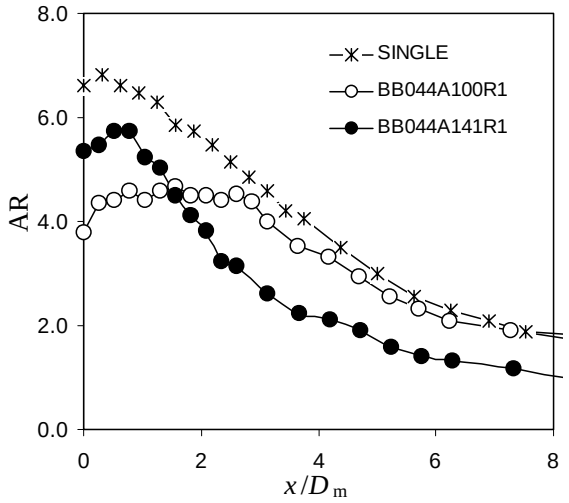

Figure 19: Evolution of aspect ratio. Comparison between MESPI case with two coflows, reference case, and SINGLE jet.

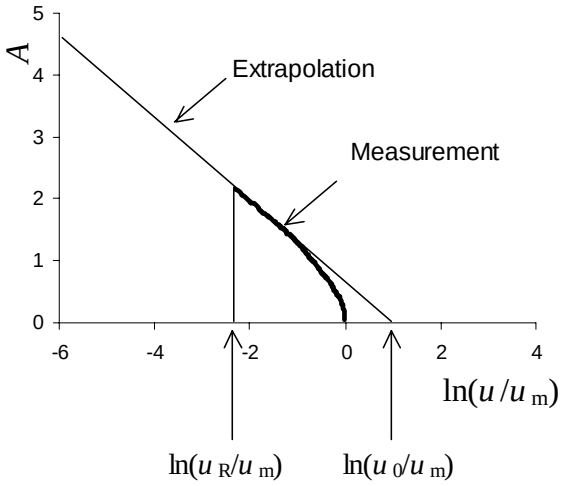

Figure 21: Relation between velocity u and area A enclosed by the isocontour of u.

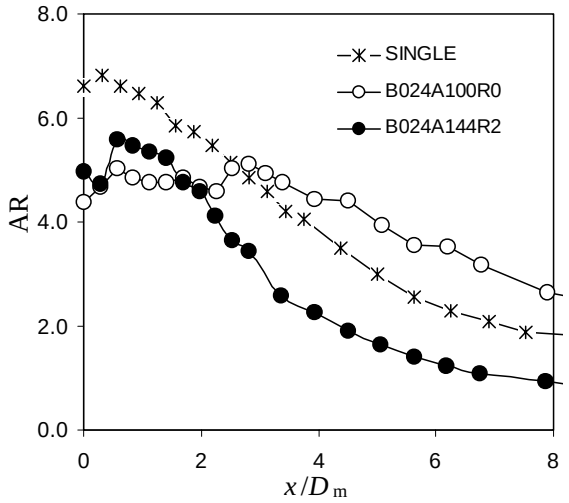

Figure 20: Evolution of aspect ratio. Comparison between MESPI case with one coflow, reference case, and SINGLE jet.

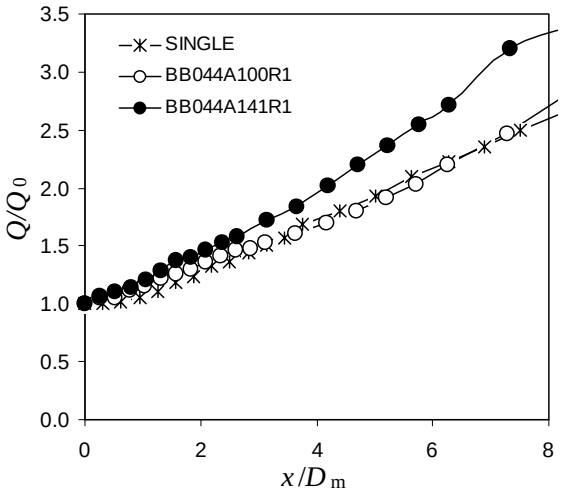

Figure 22: Evolution of volume flow rate. Comparison between MESPI case with two coflows, reference case, and SINGLE jet.

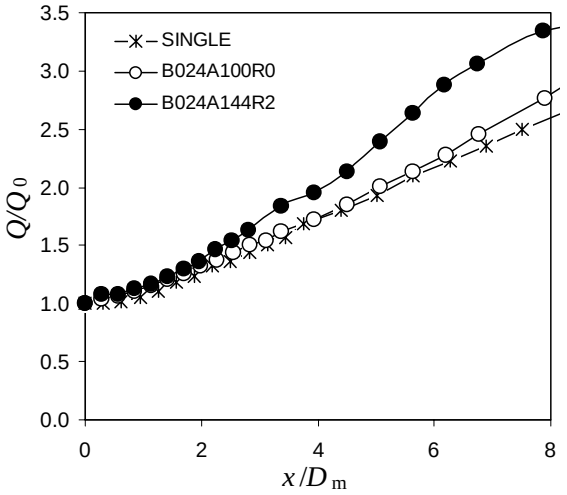

Figure 23: Evolution of volume flow rate. Comparison between MESPI case with one coflow, reference case, and SINGLE jet.

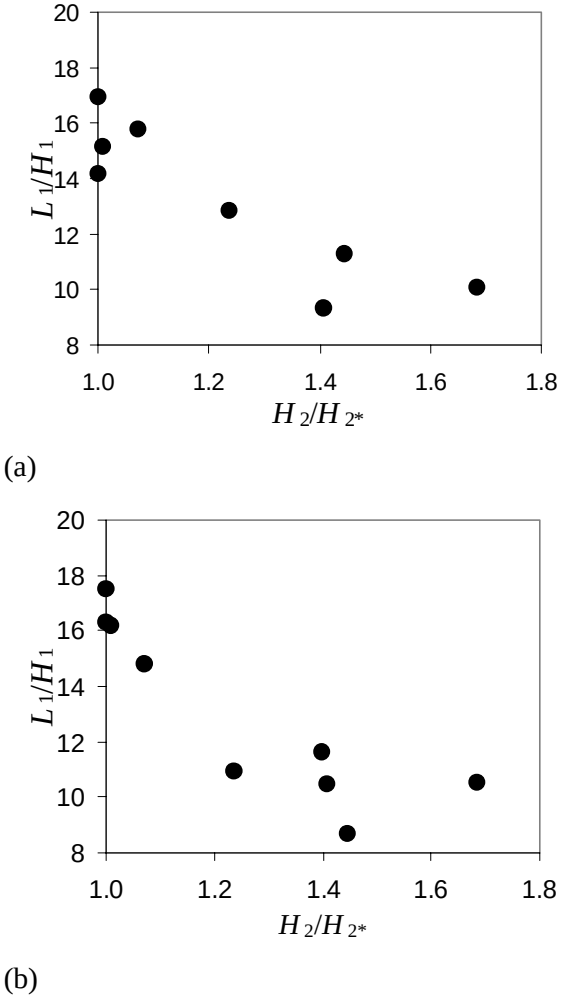

Figure 24: Correlation between potential core length and area ratio of coflow. (a) Cases with two coflows; (b) cases with one coflow.

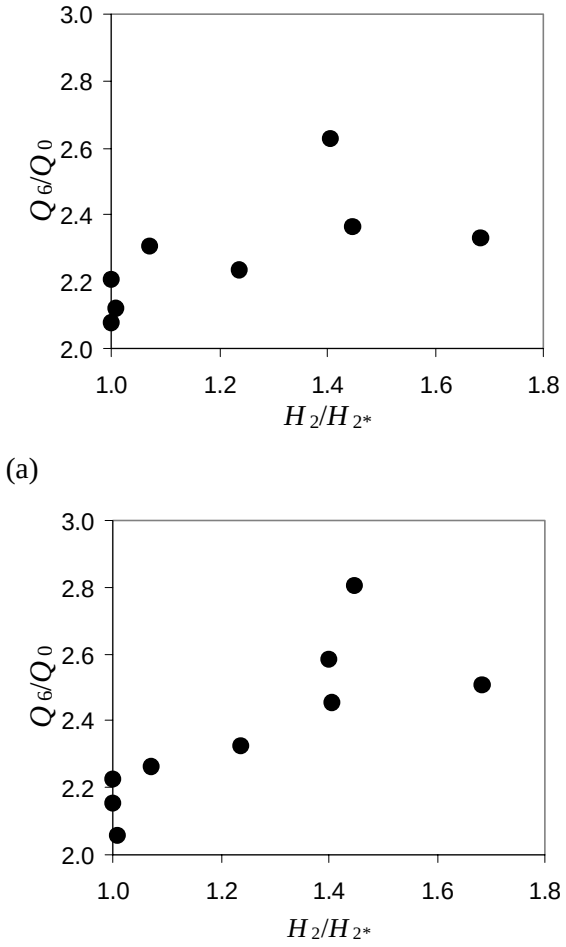

Figure 25: Correlation between volume flow rate at $x/D_m = 6$ and area ratio of coflow. (a) Cases with two coflows; (b) cases with one coflow.

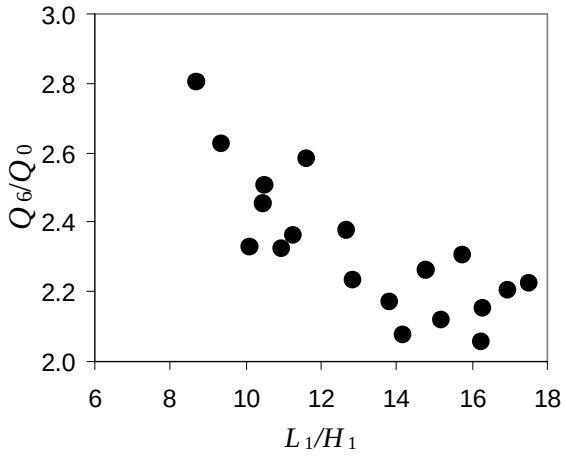

Figure 26: Correlation between potential core length and volume flow rate at $x/D_m = 6$. All cases.

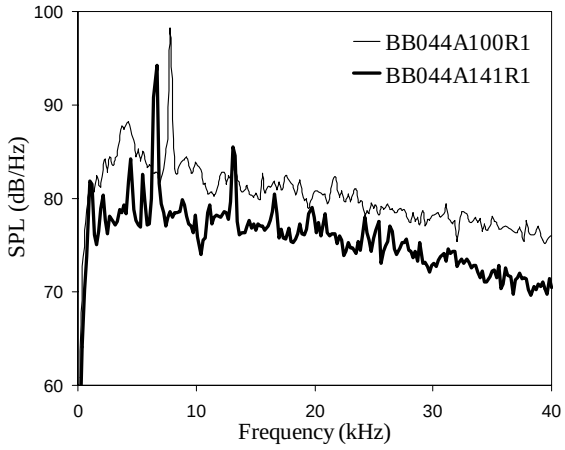

Figure 27: Noise spectra of reference and MESPI cases with two coflows.

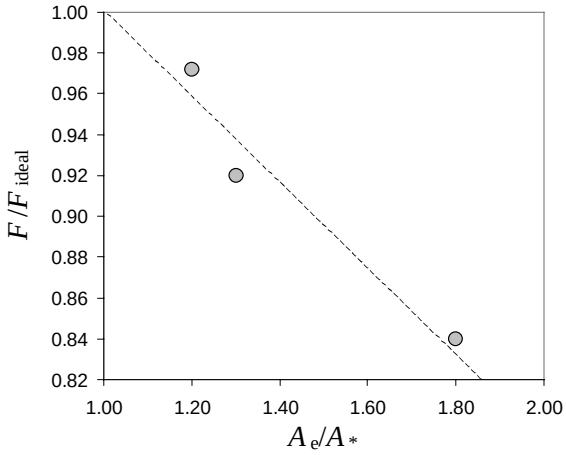

Figure 28: Thrust coefficient versus area ratio for nozzle pressure ratio 2.0. Experimental data are from [6] for A_e/A_*=1.2; [7] for A_e/A_*=1.3; and [8] for A_e/A_*=1.8. Dashed line is least-squares fit. This plot applies to the *coflow only* of the MESPI jets.